ce/papers Proceedings in civil engineering

Ernst & Sohn A Wiley Brand

ORIGINAL ARTICLE

ibausil F. A. Finger-Institut für Baustoffkunde Bauhaus-Universität Weimar

Multidisciplinary approach for the prediction of cement paste rheological properties:

physical analysis, experimental rheology and microstructural modelling

Mareike Thiedeitz[1] | Claudia Crasselt[2] | Peng Xiao[3] | Neven Ukrainczyk[3] | Wolfram Schmidt[2] | Thomas Kränkel[1]

Correspondence

Mareike Thiedeitz
Centre for Building Materials
Technical University of Munich
Germany
Franz-Langinger-Straße 10
81245 München
Email: mareike.thiedeitz@tum.de

[1] Technical University of Munich, Germany; TUM School of Engineering and Design, Department of Materials Engineering, Center for Building Materials, Chair of Materials Science and Testing
[2] Bundesanstalt für Materialforschung und -prüfung, Germany
[3] Technical University Darmstadt, Germany

Abstract

In this contribution, an interdisciplinary approach was employed to investigate and describe the fresh rheology of cementitious pastes, using analytical techniques, microstructural modelling, and experimental rheometry. The pastes, based on Ordinary Portland Cement and Limestone Calcined Clay Cement at a solid volume fraction of $\Phi = 0.45$, were subjected to various analyses. Physical and chemical analyses were conducted including laser granulometry and isothermal heat flow calorimetry. Dynamic rotational rheometry and static oscillatory rheometry, along with viscoplastic and viscoelastic rheological modelling were used to support the characterization of the pastes. A physics-based Monte-Carlo algorithm was developed to numerically describe rheological properties such as structural buildup and yield stress. The results showed that as the physical properties of the pastes became more complex, the correlation of several analysis methods went more challenging. However, the combination of analytical, experimental, and phenomenological rheology allowed for a more distinct characterization of the cement paste. These findings can serve as a basis for further multidisciplinary rheological characterization of cementitious building materials.

Keywords

Cementitious materials, fresh state rheology, cement paste, flowability, Monte-Carlo particle based modelling

1 Introduction

The time- and shear-dependent change of rheological parameters is an ongoing topic of investigation in concrete rheology since more than 100 years. For an accurate prediction of concrete rheology and its associated flow and form filling behavior, a clear and scientific understanding of the time- and shear-dependent evolution of its paste viscoplastic and viscoelastic deformability as well as its structural buildup is key. Rheological properties of cementitious systems are mainly affected by their physical and chemical particle interactions, which holds true particularly for dense packed concretes, for systems with a rapidly changing consistency demand (additive manufacturing or shotcrete applications) or for low-carbon systems with significant amounts of supplementary cementitious materials (SCMs). However, rheological characterization gets more complicated. The frequently used Bingham model ($\tau = \tau_0 + \mu * \dot{\gamma}$, [1]) does not account for non-linearities such as shear-thinning or shear-thickening or viscoelastic properties. Furthermore, structural buildup measurements require precise investigation. With decreasing particle diameters and increased use of admixtures, structural buildup (which composes of reversible physical-based thixotropy and non-reversible chemical hydration), cannot be neglected but requires a distinct investigation and calculation. Combining experimental rheometry and analytical or numerical methods supports the understanding of the causes for certain rheological performances and, in the end, decreases the need for extensive experimental laboratory programs to adjust the rheological properties. However, the correlation of chemical composition, physical properties and rheology is not straightforward. Flatt et al. described a correlation between these properties and the plastic yield stress through the YODEL model for concentrated multimodal suspensions [2]. Even if it does not apply to cementitious suspensions directly, application for cementitious pastes and a shifting factor approach to non-measurable cementitious pastes were investigated by

https://doi.org/10.1002/cepa.2812

Mantellato and Flatt in [3]. More complex numerical approaches to not only describe a plastic yield stress but also structural buildup have been employed by Hattori and Izumi in [4] or Wallevik in [5]. However, cement paste research still lacks fundamental knowledge and straight-forward approaches to correlate complex rheological behavior of cementitious paste and chemical and physical properties, and, in addition, to merge them in applicable numerical modelling.

Thus, the aim of the present research is to achieve a general understanding of combined viscoplastic, viscoelastic and structural buildup rheological behavior of cementitious paste by considering the impact of agglomeration over time, by using experimental and numerical methods. The research serves as basis for prospective effective and robust numerical modelling to predict more complex cement rheology in dependence of its physical and chemical composition.

2 Materials and methods

2.1 Concept of the investigation

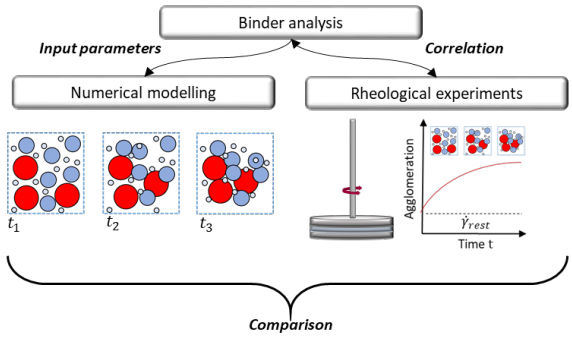

Figure 1 Concept of multi-disciplinary rheology: Correlation of analytical techniques, numerical modelling and rheological experiments

Two binders were investigated: Ordinary Portland Cement (OPC, Heidelberg Cement, Germany) CEM I 42.5 R acc. DIN EN 197-1 [6] was used as reference binder. The second binder is a Limestone Calcined Clay Cement (LCCC), a compound of 51.9% CEM I 42.5 R, 15.6% limestone powder (LS), 2.5% anhydrite and 30.0% calcined clay (CC) by volume. This mixture is of high interest as it refers to the new low-carbon cement LC^3 developed at the institute EPFL STI IMX LMC (https://lc3.ch). The materials are part of the DFG SPP 2005 program [7], data in brief of the materials are published in [8]. Pastes with a solid volume fraction of $\Phi = 0.45$ were prepared, the mixture compositions are given in Table 1.

Table 1 Mixture proportion

Series	w/b ratio[1]	Binder	Water	Paste density
[-]	**[-]**	**[kg/m³]**	**[kg/m³]**	**[kg/m³]**
CEM-0.45	0.40	1,399	550	1,950
LCCC-0.45	0.42	1,295	550	1,850

[1] In case of LCCC mixes, the whole composite (CEM + LS + CC) was taken for w/b calculation

2.2 Analysis of cementitious pastes

Isothermal heat flow was recorded using a TAM Air calorimeter (TA Instruments) to monitor the hydration process and to evaluate the effect of the SCMs. Pastes were prepared according to chapter 2.1 and after mixing 4.2 g of paste samples were placed in plastic vessels into the calorimeter at 20°C.

To provide parameters for the physics based numerical model, particle size distributions (PSD) at different times in early hydration were analysed by laser granulometry. The laser diffraction HELOS/BR series in connection with the wet dispersion system SUCELL (Sympatec GmbH), with an optical range of 0.1–875 µm, was used for the investigations. The material was dispersed with ultrasound in 2-propanol.

Samples for PSD measurements were prepared as follows. At 15 and 30 minutes after initial water addition, a small amount of paste was taken from the mix and the hydration was stopped immediately by water-solvent exchange with 2-propanol, similar to the procedure described in Scrivener et al. [9] With this method, however, particles smaller than the filter retention (2 µm) are lost. To take all particles into account, the filtrate was decanted, and the sediment was also collected. The material then was dried and stored in a vacuum oven at 23 °C.

2.3 Rheological characterization

An MCR 502 rheometer (Anton Paar, Germany) was used to measure viscoplastic, viscoelastic and thixotropic material parameters of the cementitious pastes. All pastes were mixed for a total of 90 sec with a four-bladed drilling machine at 1900 min^{-1}, followed by a resting time until 12:30 after water addition. After an additional shear up of 30 sec, pastes were applied to the rheometer and the rheological test started 15 min after water addition. Viscoplastic material parameters were studied through dynamic shear rheology using parallel plates with d= 50 mm and serrated surfaces to prevent wall slip. The gap between the plates was 1 mm. Rheological parameters, i.e. the dynamic yield stress $\tau_{d,H-B}$ and apparent viscosity η were calculated using the Herschel-Bulkley regression:

$$\tau(\dot{\gamma}) = \tau_{0,dH-B} + k * \dot{\gamma}^n \qquad (1)$$

Oscillatory structural buildup measurements require the adjustment of an imposed strain in the non-destructive regime, wherefore Large Amplitude Oscillatory Shear (LAOS) measurements were applied to the pastes before testing the structural build up. By increasing the strain amplitude and measuring the resulting stress, the change from the non-destructed linear-viscoelastic plateau region to increasingly broken particle bonds can be observed precisely. A strain amplitude from $\gamma = 1 * 10^{-3}$ to $\gamma = 1 * 10^{2}$ % was applied to the pastes; and the resulting storage modulus G' [Pa] and loss modulus G'' [Pa] were observed. The linearity limit γ_l [%] was defined at 10% deviation of G' from the plateau value at the linear viscoelastic regime (LVE), as schematically illustrated in Figure 2.

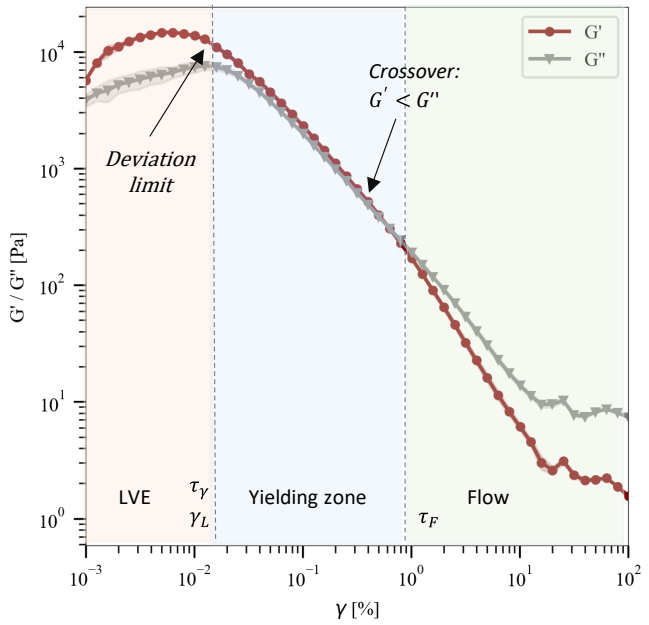

Figure 2 Schematic yielding regions with illustration of deviation limit after LVE, crossover point

The corresponding yield point τ_y [Pa] was calculated acc. the Hookean law:

$$\tau_y = G^* * \frac{\gamma_l}{100} \quad (2)$$

G^* is the complex shear modulus [Pa], and calculated as $\sqrt{G'^2 + G''^2}$. The yield point τ_y does not directly correspond to the dynamic yield stress $\tau_{0,H-B}$, as it is calculated when first agglomerate bond destruction is measured instead of extrapolating a phenomenological flow curve expression as in eq. (1). τ_y therefore is lower than $\tau_{0,H-B}$. Further chemical and physical relation can be found in [10], application of the comparison between τ_y and numerical modelling by Ukrainczyk et al. in [11]. To investigate structural buildup or agglomeration processes, the static oscillatory buildup test was performed at a strain lower than γ_l and the evolution of G' and G'' was observed for a structural buildup time of 20 min. The increase of storage modulus G' was fitted to the approach proposed by Ma et al. in [12]:

$$G`(t) = c * \left[1 - e^{-t/\theta}\right] + G_{rigid} * t \quad (3)$$

With $G`(t)$ as storage modulus with time [Pa], c as structural parameter during the nonlinear percolation [Pa], θ as percolation time [s] and G_{rigid} as linear rigidification rate [Pa/s].

2.4 Particle modelling

Particle modelling is based on the Monte Carlo method for 3D off-lattice situation to simulate the particle aggregation process in the MATLAB commercial software. The model can be divided into the following parts:

- Spherical particles are randomly placed within a cubic container of a certain volume without overlap. Depending on the actual research goal, input parameters mainly include temperature, particle size distribution, particle number, and solid volume fraction.
- Random particle movement: individual particles can be selected and move randomly in any direction and distance. Particles within clusters can also be moved. During this process, two crucial control parameters need to be emphasized: the probability of a particle being selected (determined by temperature, the proportion of single particles, and cluster size), and the probability of particle movement (determined by temperature, solid volume fraction, and energy change of the system).
- Particle aggregation: When particles are in close proximity, they may aggregate, with the probability determined by the solid volume fraction, the size of the two particles or clusters, temperature, and the balance between attractive and repulsive forces. After considering the attractive and repulsive forces, the equilibrium positions that can be reached between the particles are chosen based on the DLVO theory and determined probabilistically in the range of 5-20 nm. The model updates all system parameters in real-time after each movement and aggregation event, ensuring the timeliness of the physical background within the system.

The output results include a fully resolved 3-dimensional analysis of the number and size distribution of clusters (which can be compared with the experimental particle size distribution), the system's energy change, and the microscopic structure (aggregation morphology, pore size distribution, crosslinking situation, etc.). To establish a connection with rheological characteristics, we assume that after aggregation occurs, the resistance to small-angle shear forces applied to the sample surface is mainly provided by the aggregated parts. The aggregation process with time is mainly characterized by two parameters: the Connection Ratio CR as the volume ratio of particles contained in the aggregated parts that span the system), eq. (4):

$$CR = A \cdot \frac{V_{con}}{V_{tot}} \quad (4)$$

Where V_{con} is the volume of all particles forming the aggregated parts that span the research system, V_{tot} is the volume of the whole system, and A as an adjustment parameter. The Cumulative Coordination Number CCN is the total number of the interaction forces between particles of different sizes within each size group that undergo aggregation [2]), see eq. (5)

$$CCN = B \cdot \sum_i CN \quad (5)$$

With *B* as adjustment parameter, *i* as the number of diameter groups.

In Figure 3, the spheres marked in green represent individual particles that have not yet aggregated, while the blue-marked spheres denote aggregated particles forming clusters. Some of these clusters are highlighted in red, signifying that at least one particle within these clusters is in contact with the cubic surface. The red-framed section in

(c) illustrates a cluster connecting two corresponding faces within the cubic, (for ease of observation, the interparticle distance has been increased to twice its original value, while the particle size remains unchanged). In (d), two clusters are selected for examination and determination of the coordination number. Initially, particles of varying sizes are grouped according to their diameters. Subsequently, a scan is performed within each cluster, documenting the bonding count for each diameter group, and generating a corresponding table.

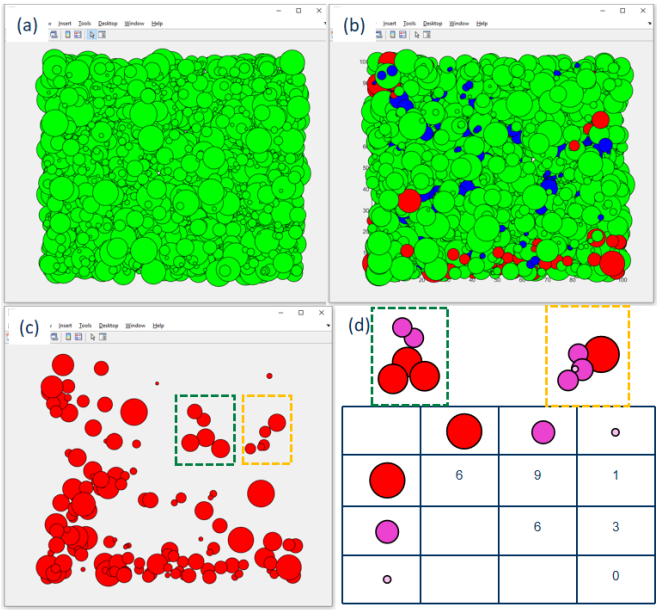

Figure 3 *Schematic illustration of the OPC aggregation process (top view). (a) shows the particle distribution at 0 minutes, (b) and (c) display the particle distribution at time t, (d) represents how to find the Coordination Number CN.*

The analysis of CR and CN with increasing agglomeration time; and the multiplicative relationship between these two parameters and the probability of bonding plays a decisive role in the resistance against shear forces.

3 Results

3.1 Chemical and physical analysis

Heat flow curves of OPC and LCCC pastes are shown in Figure 4. After the initial dissolution, the OPC-0.45 paste exhibits three peaks in the heat flow during the main hydration (labelled in Figure 4). The first peak can be assigned to the silicate reaction. The second and third peak refer to aluminate reactions after the solid sulphate depletion, whereas the second peak marks the second dissolution of C_3A and the corresponding ettringite formation, and the third peak the formation of monosulphate.

For the LCCC-0.45, the duration of the induction period is approximately the same as for OPC-0.45, thus, the onset of the acceleration stage for both mixes is comparable. Moreover, the main hydration peak of the LCCC-0.45 occurs roughly at the same time as the C_3S reaction peak in the OPC-0.45 mixes. In contrast, the aluminate reaction is not very pronounced in the heat flow curve of the LCCC-0.45 and, in addition, is retarded for several hours compared to the OPC-0.45. This is due to the additional sulphate in the LCCC-0.45 and moreover, the aluminate reacts with the limestone and so there is less transformation of ettringite into monosulphate after the sulphate depletion. The small peak at the later stage of the LCCC-0.45 hydration represents the reaction of calcined clay and limestone.

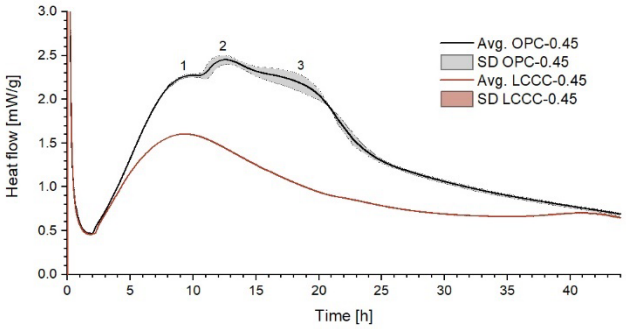

Figure 4 Average (Avg.) heat flow curves with standard deviation (SD) of ordinary Portland cement (OPC) and limestone calcined clay cement (LCCC) pastes.

Particle size distributions of ordinary Portland cement (OPC) and limestone calcined clay cement (LCCC) at different times of hydration listed in Table 2 and Table 3, and shown in Figure 5 and Figure 6.

In OPC-0.45 pastes, the particle size distribution does not change equally during hydration but varies in different fractions. The smallest (< 0.4 µm) and the 2 - 12 µm fraction decreases, while the 0.4 - 2 µm and 12 -35 µm fractions increase with hydration time. Only after 30 minutes there is an increase in larger particles over 35 µm. The median particle size (D50) increases with hydration and at 30 minutes the mode is also shifted towards higher particle size. The D10 and D90 percentile particle sizes first decrease at 15 minutes and then increases at 30 minutes. Altogether, a shift to higher particle sizes is apparent from the cumulative particle size distribution.

Table 2 Mean particle size distribution ordinary Portland cement (OPC) at 0, 15 and 30 minutes of cement hydration.

Series	Time	D10	σ	D50	σ	D90	σ
	[min]	**[µm]**	**[µm]**	**[µm]**	**[µm]**	**[µm]**	**[µm]**
OPC-0.45	0	2.20	0.03	13.46	0.27	39.16	0.49
	15	2.02	0.14	13.93	0.22	38.38	1.15
	30	2.30	0.20	15.56	0.59	41.39	1.10

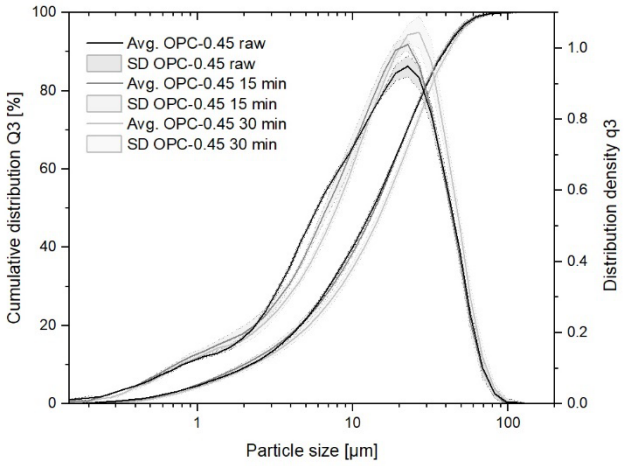

Figure 5 Average (Avg.) particle size distributions and standard deviations (SD) of ordinary Portland cement (OPC) at different times of hydration.

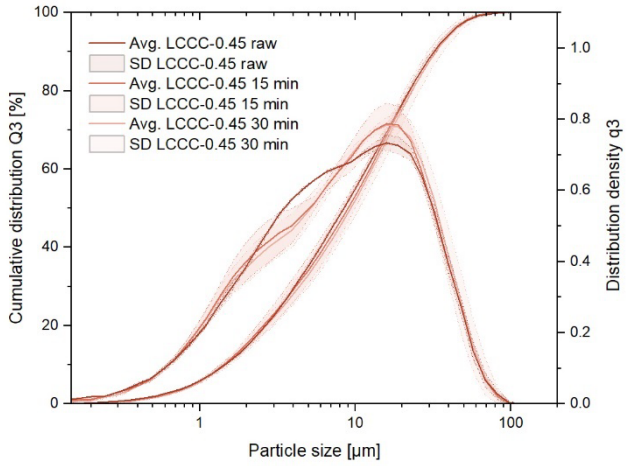

Figure 6 Average (Avg.) particle size distributions and standard deviations (SD) of limestone calcined clay cement (LCCC) at different times of hydration.

The particle size distribution of the LCCC-0.45 is more bimodal than that of the OPC-0.45. Particle sizes in the LCCC-0.45 are generally smaller and also have a greater proportion of smaller particle fractions. During hydration the smallest (< 0.5 µm) and distinctly the 2 - 9 µm fraction decreases, while the 0.5 - 2 µm and 9 -30 µm fractions increase. An increase in larger particles (> 30 µm) is only visible after 30 minutes of hydration. The median particle size (D50) increases with hydration, and the D10 and D90 percentile particle sizes again first decrease at 15 minutes and then increase at 30 minutes, and therefore show the same trend as the OPC-0.45 pastes. For the LCCC-0.45 also a slight shift to higher particle sizes is apparent from the cumulative particle size distribution. However, this shift is less pronounced compared to the OPC-0.45 and also the mode is not shifted to higher particle size. Further, the difference from 15 to 30 minutes is in general less for the LCCC-0.45 than for the OPC-0.45, but a notable decrease between 2 and 9 µm is visible, which is not apparent for the OPC-0.45.

Table 3 Mean particle size distribution of limestone calcined clay cement (LCCC) at 0, 15 and 30 minutes of hydration.

Series	Time	D10	σ	D50	σ	D90	σ
	[min]	**[µm]**	**[µm]**	**[µm]**	**[µm]**	**[µm]**	**[µm]**
	0	1.46	0.04	8.44	0.13	32.15	1.16
LCCC-0.45	15	1.43	0.08	9.01	1.02	32.07	1.29
	30	1.48	0.09	9.44	1.24	33.05	3.80

3.2 Flow curves

Each paste was analysed at minimum three times. Detailed information on the test geometries, mixing protocols and raw data handling can be found by Thiedeitz et al. in [13]. The average raw data and standard deviations to analyse rheological flow parameters yield stress τ_0 and apparent viscosity η value are plotted in Figure 7.

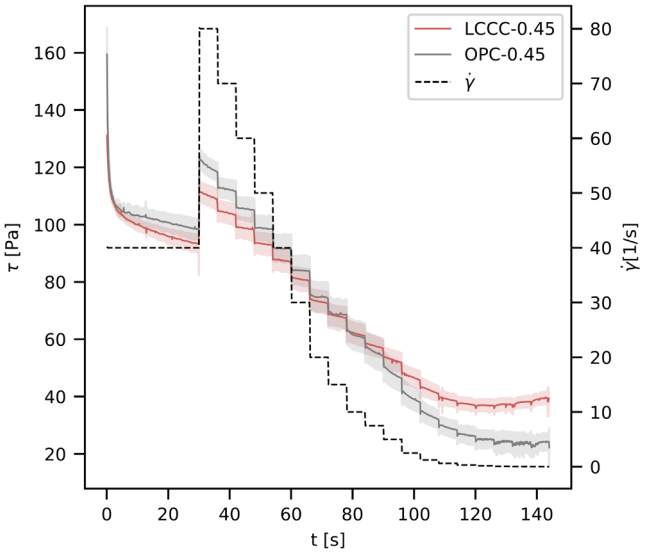

Figure 7 Raw data: Shear stress measurement of OPC-0.45 and LCCC-0.45

The average shear stress τ after equilibrium was calculated for each shear rate $\dot{\gamma}$, and the corresponding dynamic τ - $\dot{\gamma}$ flow curves are plotted in Figure 8. The Herschel-Bulkley regression (see eq. (1)) was used to calculate rheological parameters.

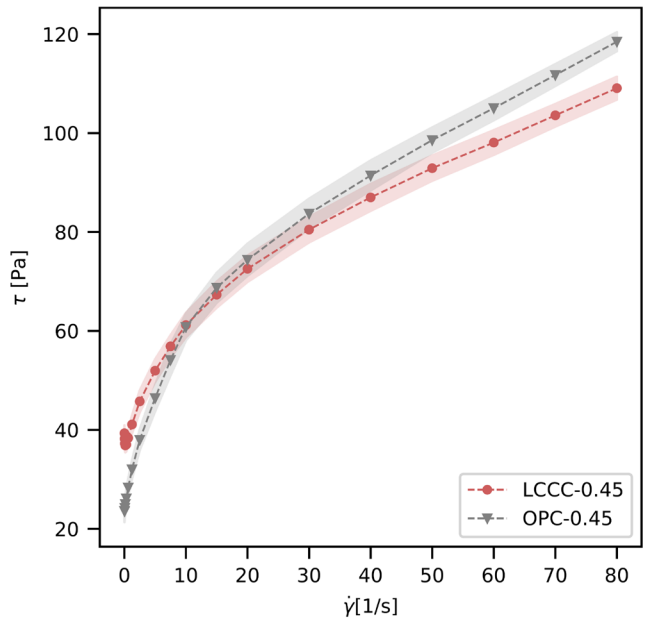

Figure 8 Average dynamic τ - $\dot{\gamma}$ curves with standard deviations of OPC and LCCC

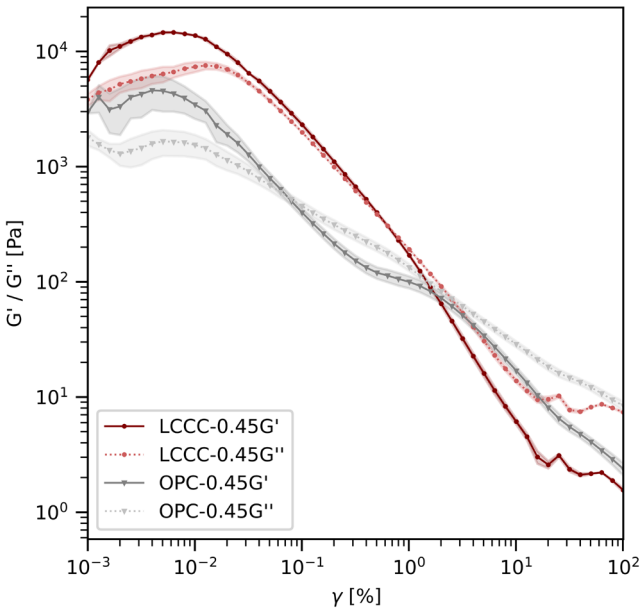

Figure 9 Non-destructive large amplitude oscillatory shear tests

The viscoplastic parameters for both series OPC-0.45 and LCCC-0.45 are given in Table 4. The LCCC-0.45 possesses a higher dynamic yield stress τ_{H-B} through Herschel-Bulkley regression, Figure 8 shows that OPC-0.45 has a slightly higher inclination of the $\dot{\gamma} - \tau$ – curve, which is a measure of viscosity at increasing shear rates. Non-Newtonian indices of both test series are similar, however LCCC-0.45 possesses a higher non-Newtonian index n (even though both pastes are clearly shear-thinning).

Table 4 Viscoplastic parameters

Series	Viscoplastic analysis		
	$\tau_{0,H-B}$	k	n
	[Pa]	**[Pas^{-1}]**	**[-]**
OPC-0.45	17.3	15.4	0.43
LCCC-0.45	29.4	11.2	0.45

Material behaviour at rest is analysed through the Large Amplitude Oscillatory Sweep (LAOS) with an amplitude starting at rest; followed by structural buildup measurement for 15 min at a previously determined non-destructive amplitude.

Figure 9 displays the LAOS curves. At rest or low deformation, the LCCC-0.45 particle structure is more stable and contains more viscoelastic energy (see red curves LCCC-0.45G' in Figure 9, with a storage modulus G' at the linearity plateau of 10,960 Pa, see Table 5), which corresponds to the results from the dynamic shear measurement. The yield point γ_l is at a slightly higher deformation γ for LCCC-0.45; and τ_Y is higher (see calculated values in Table 5).

Figure **10** shows the structural buildup in a non-destructive oscillatory test, with the oscillating strain γ below γ_l (set to $\gamma_l = 5 * 10^{-3}$ %). The rheological test started 15 min after water addition, so the x-axis in Figure **10** starts at 0 min measuring time, which is equal to 15 min after water addition. Structural buildup evolves faster and at a higher rigidification rate G_{rig} for LCCC-0.45 pastes. After initial flocculation, structural buildup increases at a similar rate for OPC-0.45 and LCCC-0.45.

It has to be noted that both test series were relatively instable in the first seconds of the rheological test, as visible by several outliers. This is due to the relatively high water/cement ratio in the suspension, which leads to unstable pastes and thus high measuring sensitivity. Agglomeration and rigidification over time however led to stable pastes with increasing storage moduli G'. Viscoelastic and structural buildup parameters are given in Table *5*.

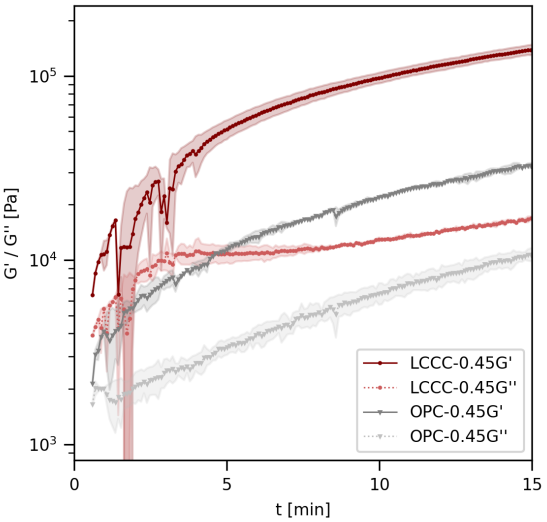

Figure 10 Evolution of storage modulus G' and loss modulus G'' for LCCC-0.45 and OPC-0.45

Table 5 Viscoelastic parameters and structural buildup

Series	G'_{LVE}	γ_l	τ_y	G_{rid}
	[Pas]	[%]	[Pa]	[Pa/s]
OPC-0.45	3,450	0.010	0.38	37.3
LCCC-0.45	10,960	0.016	2.11	141.27

3.3 Numerical modelling

From Figure 11, we can observe that as time progresses, both CR and CCN exhibit a growing trend. For OPC-0.45 and LCCC-0.45 the CR initially increases rapidly and then levels off, while the CCN demonstrates an almost linear growth trend. Comparing OPC and LCCC samples, there is no significant difference in trends of CR, but the CCN for LCCC grows more significantly.

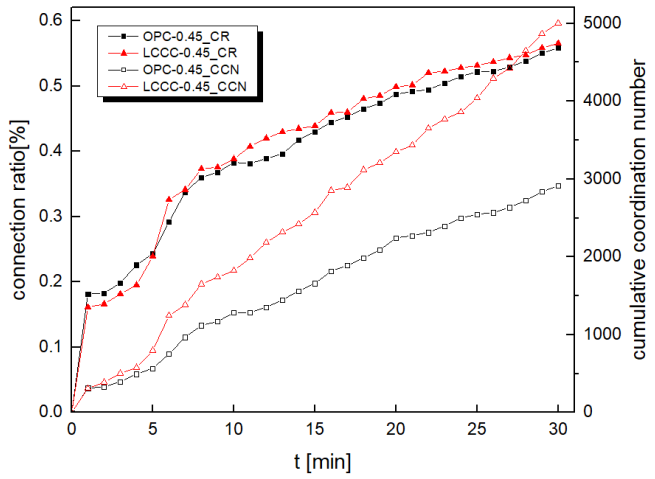

Figure 11 Evolution of CR and CCN over time

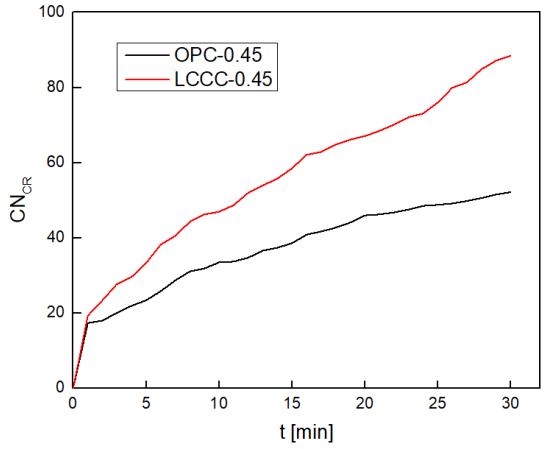

Figure 12 Preliminary prediction of storage modulus over time

In the proposed model, the shear stress τ applied on the cubic surface is resisted by the bonding probability within the cubic, CN, and CR, as shown in Equation 6.

$$G' = \kappa \cdot \sum_i P \cdot CN_{CR} \cdot CR \qquad (6)$$

$$CN_{CR} = \frac{CCN}{CR \cdot N_p \cdot \frac{V_{tot}}{V_p}} \qquad (7)$$

Where k is the adjustment parameter with unit, N_p is the total number of particles; V_p is the total volume of particles. The expressions for bonding probability, as well as the numerical analysis of CCN and CR, are still in progress. In the present work, the entire CCN is assumed to be used for the CR within the system, i.e., calculating the average number of interaction forces between particles with at least one contact point formed, shown in eq. (7). The value of CN_{CR} with time has been plotted in Figure 12 to investigate its relationship with G'. The vertical axis in Figure 12 does not have practical units due to the lack of control of adjusted parameters.

The predictions reveal that G' increases rapidly in the initial stages of agglomeration and then gradually enters a plateau phase, a feature particularly evident in OPC. The plateau phase for LCCC is not as apparent, which is related to the faster growth of CCN in LCCC shown in Figure 11. With increasing hydration time, particle size distribution changes, which means less agglomeration forces.

Since the model is currently undergoing further optimization, the vertical axis shown in Figure 13 represents the normalized frequency of particles appearing in each diameter group and does not have actual units. For OPC-0.45, from 0 to 15 minutes and then to 30 minutes, the peak gradually shifts to coarser particle fractions. In contrast, for LCCC-0.45, a noticeable peak shift can be observed at 15 minutes, but the shift from 15 to 30 minutes is not as pronounced. Relative to LCCC-0.45, the three peaks of OPC-0.45 are narrower, indicating a more concentrated particle size distribution. These features are consistent with the actual test results shown in Figure 5 and Figure 6, which demonstrates the reliability of the model.

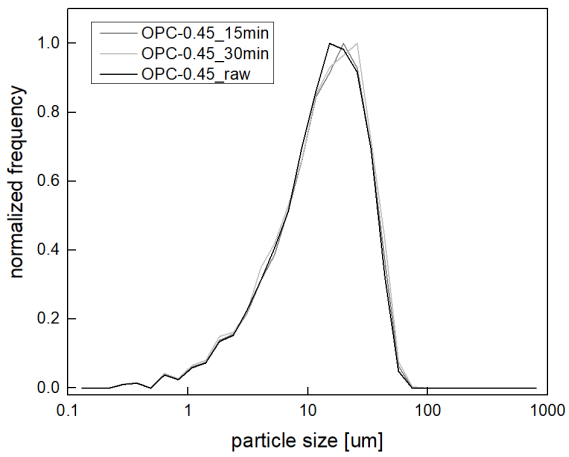

Figure 13 Numerical Particle Size Distribution at 0, 15 and 30 min for OPC-0.45

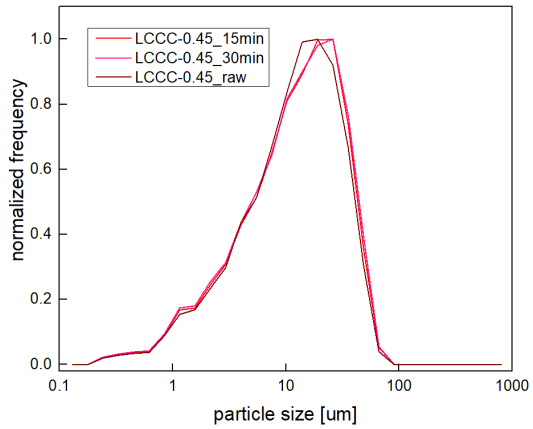

Figure 14 Numerical Particle Size Distribution at 0, 15 and 30min for LCCC-0.45

3.4 Correlation of experimental and numerical particle size distribution

Combined experimental and numerical results of particle size distributions at different hydration times are shown in Figure 15 and Figure 16 for OPC-0.45 and LCCC-0.45, respectively.

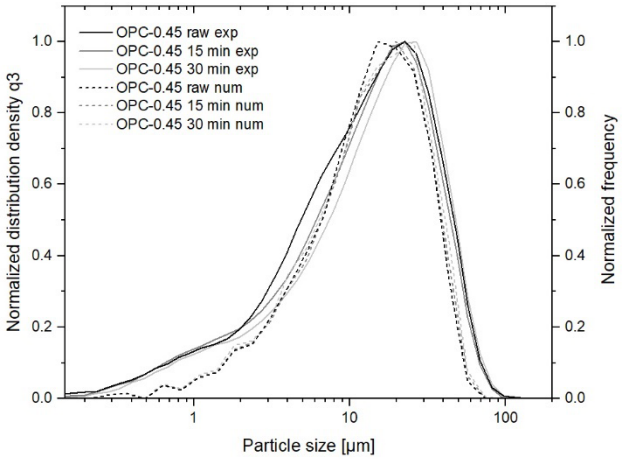

Figure 15 Combined numerical (num) and experimental (exp) particle size distributions of ordinary Portland cement (OPC) at different times of hydration.

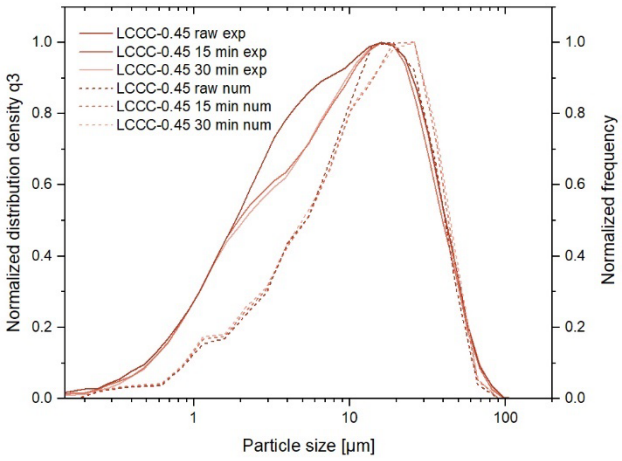

Figure 16 Combined numerical (num) and experimental (exp) particle size distributions of limestone calcined clay cement (LCCC) at different times of hydration.

The numerical particle size distribution of the raw material does not fully agree with the experimental results. One main reason for this is that the fitting equation used to input the starting material data from the experiments as a reference for the model is not yet accurate enough with an R-value of only 0.9, leading to some systematic errors in the input data. Two further reasons may account for the deviation: First, the numerical input and output uses fewer data points than laser granulometry, which leads to less continuous simulation results, and second, the current model does not consider the porosity included within the clusters when calculating the size. However, the particle cluster model already provides a good approximation and fit of the particle size distributions, as can be seen from the combined results.

For the OPC-0.45 the smaller fraction is a little underrepresented in the numerical results and the larger fraction has a slight offset to smaller particle size. But the gradual shift to higher particle size fits the experimental results very well. In the numerical results this shift is most obvious for the mode, while in the experimental results this is visible also in other fractions. The particle size distribution for OPC-0.45 is more mono-modal and narrower than the LCCC-0.45, which is consistent with the experimental results.

In the numerical size distribution of LCCC-0.45 the smaller fraction is again underestimated, but the fraction from 1 to 10 µm is also underrepresented. Possible explanations for that have already been mentioned above. This also might account for the discrepancy in the fractions of LCCC-0.45 that are shifted. In the experimental results the biggest shift during hydration occurs in the 2 – 9 µm fraction, whereas in the numerical results the biggest shift occurs in the 9 – 25 µm fraction. But what is consistent with the experiments, is that this shift during LCCC-0.45 hydration is not gradual like in OPC-0.45, but erratic from raw to 15 minutes. For higher particle size the model gives a very good fit.

In terms of particle size distribution simulation, the model requires improvement in the following points to address the issues encountered. Further code needs to be implemented to calculate the distribution of porosity and a more suitable fitting equation must be found. In addition, the number of data points should be increased, and the most appropriate periodic condition must be found.

3.5 Correlation of rheology and Monte Carlo simulation

Figure 17 presents the combined results of experimental and numerical modelling for structural buildup. The storage modulus increase, $G'(t)$, was plotted for rheological experiments, while the coordination number CN, was shown for numerical results. It is important to note that the experimental rheological experiment began 15 min after water addition, whereas the numerical simulation tracked agglomeration immediately after initial contact with water. As immediate rheological measurements are not feasible or meaningful, structural buildup analysis was followed experimentally starting from 15 min after water addition, with pre-shearing to de-flocculate already built networks.

On the other hand, numerical modelling was able to address agglomeration within a fixed time frame, and thus, agglomeration was initially modelled.

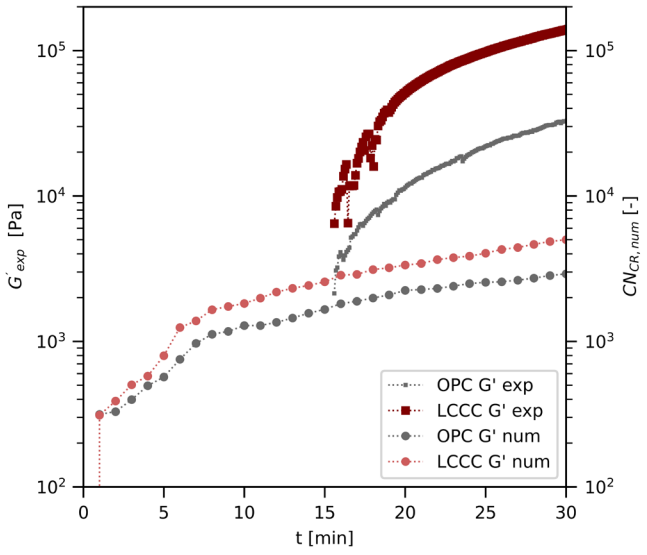

Figure 17 Combined numerical (num) and experimental (exp) structural buildup analysis for OPC-0.45 and LCCC-0.45 within a timeframe of 15 min

As shown in Figure 17, the numerical results demonstrate a correlating trend with the experimental data, albeit with a time shift between both. The initial high agglomeration observed in both experimental and numerical data reveals the tendency of cementitious suspensions to agglomerate at a higher rate when smaller clusters are available (as smaller particles move faster), and the agglomeration rate gradually approaches a plateau with increasing time and higher cluster values (due to higher inertia of the bigger particles). In addition, higher CN values obtained from numerical agglomeration analysis correspond to higher storage moduli measured rheologically for the LCCC-0.45 paste. This is due to the presence of smaller particle diameters and a higher amount of fine particles (in the LCCC-0.45), resulting in a stronger network due to closer distances and 'faster' particles, in agreement with analytical data presented in sec. 3.1; and mean diameters given in Table 2 and Table 3. However, there are differences between experimental and numerical data due to the differences in numerical modelling assumptions and real experimental conditions, as well as the current limitations of the purely physical cluster model. Moreover, the difference between experiment and numerical simulation is more pronounced for LCCC-0.45 than for OPC-0.45.

In future, we plan to improve the model to accurately predict rheological properties of cementitious pastes based on both chemical and physical properties. Currently, the particle cluster model only considers physical parameters, and we do not expect perfect agreement between numerical and experimental results. However, the model's simulation of particle size distribution and the shift with ongoing hydration agrees with experimental results, indicating the physical part of the cluster model is reliable. The physical cluster model is flexible and allows for easy adjustment of various parameters to predict both particle size distribution and rheological characteristics. Our future work will focus on analysing the size of the representative elementary volumes for the Monte-Carlo simulations, finding adequate input parameters for numerical as well as simplified (upscaled) analytical models, and comparing the model with more experimental results for applicability in concrete technology practice.

4 Conclusion

Our study used an interdisciplinary approach to investigate the rheological properties and structural buildup of cementitious pastes. We combined analytical methods and experimental rheology to develop a reliable Monte-Carlo computational tool for cement particle aggregation. Although a chemical aspect has not been implemented yet, we demonstrated the model's reliability and multi-functionality. Future work will focus on analysing the optimal size for representative elementary simulation volumes, finding adequate parameters for numerical and analytical (upscaled) approaches, and comparing the model with more experimental results.

Acknowledgement. This research was funded by the National German DFG organization under project number451894070 titled "Viscoelasticity related deformability and structural build-up of fresh concrete: Effects of carrier liquid chemistry on particle interactions", as part of the DFG SPP 2005 program "Opus Fluidum Futurum—Rheology of reactive, multiscale, multiphase construction materials".

References

[1] Bingham, E. C. (1916) *An Investigation of the Law of Plastic Flow*. In: *Bulletin of the Bureau of Standards* 13, Nr. 266, p. 309–353

[2] Flatt, R. J. ; Bowen, P. (2007) *Yield Stress of Multimodal Powder Suspensions : An Extension of the YODEL (Yield Stress mODEL)*. In: *Journal of the American Ceramic Society* 90, Nr. 4, p. 1038–1044

[3] Mantellato, S.; Flatt, R. J. (2020) *Shifting factor—A new paradigm for studying the rheology of cementitious suspensions*. In: *Journal of the American Ceramic Society* 103, Nr. 6, p. 3562–3574

[4] Hattori, K.; Izumi, K. (1982) *A Rheological expression of coagulation rate threory.* In: *Journal of Dispersion Science and Technology* 3, Nr. 2, p. 129–145

[5] Wallevik, J. E. (2009) *Rheological properties of cement paste : Thixotropic behavior and structural breakdown*. In: *Cement and Concrete Research* 39, Nr. 1, p. 14–29

[6] *DIN EN 197-1:2011-11 (2011) Zement - Teil_1: Zusammensetzung, Anforderungen und Konformitätskriterien von Normalzement (EN 197-1:2011)*, Beuth, Berlin

[7] DFG *SPP 2005 (2023) Opus Fluidum Futurum - Rheologie reaktiver, multiskaliger, mehrphasiger Baustoffsysteme*. https://gepris.dfg.de/gepris/projekt/313773090 [accessed on: 21 Apr. 2023]

[8] Pott, U. et al (2023) *Characterization data of reference materials used for phase II of the priority pro-*

gram DFG SPP 2005 "Opus Fluidum Futurum - Rheology of reactive, multiscale, multiphase construction materials". In: *Data in brief* 47, pp. 108902

[9] Scrivener, K., Snellings, R., & Lothenbach, B. (Eds.). (2016). *A Practical Guide to Microstructural Analysis of Cementitious Materials* (1st ed.). CRC Press. https://doi.org/10.1201/b19074

[10] Roussel, N. et al (2012) *The origins of thixotropy of fresh cement pastes*. In: *Cement and Concrete Research* 42, Nr. 1, p. 148–157

[11] Ukrainczyk, N. et al (2020) *Modeling SAOS Yield Stress of Cement Suspensions: Microstructure-Based Computational Approach*. In: *Materials (Basel, Switzerland)* 13, Nr. 12

[12] Ma, S.; Qian, Y.; Kawashima, S. (2018) *Experimental and modeling study on the non-linear structural build-up of fresh cement pastes incorporating viscosity modifying admixtures*. In: *Cement and Concrete Research* 108, p. 1–9

[13] Thiedeitz, M.; Kränkel, T. ; Gehlen, C. (2022) *Visco-elastoplastic classification of cementitious suspensions: transient and non-linear flow analysis in rotational and oscillatory shear flows*. In: *Rheologica Acta* 61, 8-9, p. 549–570